The Astrophysical Journal, 928:173 (8pp), 2022 April 1 https://doi.org/10.3847/1538-4357/ac5a53

Accurate Metallicities for Very Metal-poor Stars from the Ca II Infrared Triplet

Yeisson Osorio[1,2,3], David S. Aguado[4,5,6], Carlos Allende Prieto[2,3], Ivan Hubeny[7], and Jonay I. González Hernández[2,3]
[1] Isaac Newton Group of Telescopes, Apto 321, E-38700 Santa Cruz de La Palma, Canary Islands, Spain; yo@ing.iac.es
[2] Instituto de Astrofísica de Canarias, Vía Láctea, E-38205 La Laguna, Tenerife, Spain
[3] Universidad de La Laguna, Departamento de Astrofísica, E-38206 La Laguna, Tenerife, Spain
[4] Dipartimento di Fisica e Astronomia, Universitá degli Studi di Firenze, Via G. Sansone 1, I-50019 Sesto Fiorentino, Italy
[5] Institute of Astronomy, University of Cambridge, Madingley Road, Cambridge CB3 0HA, UK
[6] INAF/Osservatorio Astrofisico di Arcetri, Largo E. Fermi 5, I-50125 Firenze, Italy
[7] Steward Observatory, University of Arizona, Tucson, USA
Received 2021 December 21; revised 2022 February 16; accepted 2022 March 1; published 2022 April 7

Abstract

The Ca II H and K lines are among the few features available to infer the metallicity of extremely metal-poor stars from medium-resolution spectroscopy. Unfortunately, these lines can overlap with absorption produced in the intervening interstellar medium, introducing systematic errors in the derived metallicities. The strength of the Ca II infrared triplet lines can also be measured at extremely low metallicities, and it is not affected by interstellar absorption, but it suffers significant departures from local thermodynamic equilibrium (LTE). We investigate the feasibility of adopting the Ca II infrared triplet as a metallicity indicator in extremely metal-poor stars using state-of-the art non-LTE models including the most recent atomic data. We find that the triplet lines exhibit non-LTE abundance corrections that can exceed 0.5 dex. When interstellar absorption affecting the Ca II resonance lines is accounted for using high-resolution observations, the agreement between non-LTE abundances for the triplet and those for the resonance lines, with only minor departures from LTE, is excellent. Non-LTE effects strengthen the Ca II IR triplet lines, facilitating measurements at very low metallicities, compared with LTE estimates, down to $[Fe/H] = -6.0$. This result has important implications for the discovery of primitive stars in our Galaxy and others, since instruments are most sensitive at red/near-infrared wavelengths, and tens of millions of spectra covering the Ca II IR triplet will soon become available from the Gaia, DESI, WEAVE, and PFS missions.

Unified Astronomy Thesaurus concepts: Interstellar line absorption (843); Metallicity (1031); Chemical abundances (224); Stellar surfaces (1632)

1. Introduction

The first stars born in the Galaxy inherited the composition of the pristine gas in the early interstellar medium (ISM), with basically no metals. We do not yet know whether there is a metallicity threshold for the formation of low-mass stars (e.g., Bromm & Loeb 2003; Stacy et al. 2016; Chiaki et al. 2017; Magg et al. 2018, and references therein), but there are low-mass stars with metal-to-hydrogen ratios as low as 10^{-5} (see, e.g., Ishigaki et al. 2014; Komiya et al. 2016), and even lower ratios when calcium or iron abundances are taken as a proxy for metallicity.

Very old low-mass stars that have survived until today offer us a way to track the early chemical evolution of the Milky Way and sample the nucleosynthetic yields of the first massive stars and their supernovae (e.g., Umeda & Nomoto 2005; Hartwig et al. 2018). But to do so, we first need to find suitable samples–they are truly rare, with only half a dozen known at $[Fe/H] < -5$ (Christlieb et al. 2004; Frebel et al. 2005; Keller et al. 2014; Bonifacio et al. 2015; Aguado et al. 2018a, 2018b; Nordlander et al. 2019); second, we need to learn to read their spectra, which challenge simplified models of stellar atmospheres.

At low metallicity the overall atmospheric structure is affected by the lack of metal-line absorption. This has been shown to have dramatic consequences for the formation of molecules (García Pérez et al. 2006). Lower metal-line opacity, together with a lower density due to a lower mean molecular weight, leads to a larger number of scatterings experienced by photons in spectral lines and consequently to more pronounced deviations from LTE.

At extremely low metallicities, stellar spectra, especially for warm F-type halo turnoff stars, appear void of metal lines, and only the abundances of a few elements can be measured. Searches for extremely metal-poor stars exploit the formidable strength of the Ca II H and K lines at 3934 and 3969 Å, which can be detected down to very low abundances at modest spectral resolution (e.g., Beers et al. 1985; Caffau et al. 2013; Aguado et al. 2016). However, calcium atoms in the warm ISM, with typical temperatures in the range 6000–10,000 K, are mainly sitting in the ground level of Ca II and contribute absorption in the vicinity of the stellar lines. The ISM absorption may have multiple components from individual clouds, which are narrower and usually shifted in velocity from the stellar lines. These contributions are hard to resolve and take into account when deriving stellar calcium abundances from low- and medium-resolution spectra.

The Ca II triplet lines at 8498, 8542, and 8662 Å are somewhat weaker than the resonance lines, but still fairly strong and not affected by interstellar absorption. They are in a spectral window that is nearly optimal for CCD detector efficiency, and they remain visible in a wide variety of spectral types, which has motivated their choice for Gaia's Radial Velocity Spectrograph (Cropper et al. 2018). Their use for metallicity estimation in extremely metal-poor stars has been hampered by the fact that the levels connected by the triplet are

affected by departures from local thermodynamic equilibrium (LTE), and a reliable description of the effect of inelastic collisions with atomic hydrogen was lacking and is critical. This issue has been addressed in the recent calculations by Belyaev et al. (2018).

Sitnova et al. (2019) have studied in detail the formation of calcium lines in very metal-poor stars, upgrading the model from Mashonkina et al. (2007) including the recent data for collisions with hydrogen atoms for Ca II from Belyaev et al. (2018) and those from Belyaev et al. (2017) for Ca I. The main non-LTE (NLTE) effect is an overpopulation of the lower level and photon losses in the cores of the triplet lines, which strengthens the lines. Sitnova et al. (2019) find that NLTE abundance corrections for the triplet depend mainly on line strength.

We have updated our model atoms, including the best possible collisional and radiative data, and put them to the test using existing and new, unpublished observations of several extremely metal-poor stars. Section 2 reports on the observational material. Section 3 gives an account of the atomic data, model atmospheres, and line formation calculations. Section 4 presents our results. Section 5 focus on the most metal rich star in our study: HD 122563. The last two sections focus on the three most metal poor stars in this study (Section 6) and present our conclusions (Section 7).

2. Observations

There are three sets of observations used in this work: medium-resolution spectroscopy with the Intermediate dispersion Spectrograph and Imaging System spectrograph (ISIS), on the 4 m William Herschel Telescope (WHT), and high-resolution data obtained with HORuS, installed at the 10.4 m Gran Telescopio Canarias (GTC), and the Ultraviolet and Visual Echelle Spectrograph (UVES), in operation at the Very Large Telescope (VLT).

The observations taken with ISIS span the ranges 3500–5200 Å and 7420–9180 Å and therefore cover both the Ca II H and K lines and the IR triplet at low resolution. Unfortunately, the Ca II H line (3968 Å) is not resolved in the ISIS observations. HORuS covers approximately the range between 3800 and 6900 Å, missing the infrared triplet, but allowing for a more detailed study of the H and K lines since both lines are resolved at the spectral resolution of this instrument (about 25,000). The resolving power for the UVES observations is higher ($R \sim 45{,}000$), and the spectral coverage is wider and includes the infrared triplet lines. More details are given below.

2.1. HORuS

G64-12 was observed with HORuS (Tabernero et al. 2020; Allende Prieto 2021) at GTC[8] on 2019 March 11 and July 2, HD 122563 was observed on 2020 January 13, and SDSS 134338 was observed on 2019 December 3. Data reduction was carried out with the `chain`,[9] which performs bias and flat-field correction, order tracing, extraction, and wavelength calibration. The observed spectra of the same target were combined in order to increase the signal-to-noise ratio (S/N). These spectra include some Ca I lines as well.

2.2. UVES

The high-resolution UVES (Dekker et al. 2000) spectra of HE 1327−2326 and HD 122563 were extracted from the ESO archive.[10] Radial velocities for individual spectra were determined by cross-correlation with a synthetic template, and after correcting for it, the exposures were co-added to obtain a final spectrum with an S/N of ∼120.

2.3. ISIS

Both G64−12 and HE 1327−2326 were previously studied by Aguado et al. (2017), using medium-resolution data taken at the 4.2 m WHT with ISIS (Jorden 1990). The setup included the R600B and R600R gratings with the default dichroic, allowing us to measure the Ca II H and K resonance doublet and the Ca II infrared triplet. Each target was observed for a total of 3600 s, leading to an S/N of about 300 and 130 at 3940 and 8550 Å, respectively.

3. Calculations

We carried out NLTE calculations with the latest version of `Tlusty` (version 208[11]), which can calculate NLTE populations in the trace-element approach using precomputed opacity tables, and `Synspec` (version 54[12]), which generates opacity tables and detailed LTE and NLTE synthetic spectra (Hubeny & Lanz 2017a, 2017b, 2017c; Hubeny et al. 2021).

The stellar parameters adopted for G64-12 and HE 1327−2326 were taken from Aoki et al. (2006). In the case of SDSS 134338, the parameters were calculated by some of us (Aguado et al. 2017). The parameters for HD 122563 were extracted from Heiter et al. (2015), where they obtained the parameters via bolometric flux and isochrone calibrations (see also Amarsi et al. 2016). Effects of the stellar parameters on our NLTE results are presented below.

All the synthetic spectra were calculated in the same fashion: Model atmospheres were computed afresh using the ATLAS9 (Kurucz 2005) posix port from Sbordone et al. (2007). For each model atmosphere an opacity table was constructed with `Synspec`, adopting the same abundances as the model atmosphere, but removing the contribution from Ca and Mg. The metallicity indicator we used in the calculations is the usual, [Fe/H]. It is known that in metal-poor stars [Ca/Fe] ≈ 0.4 dex, but at [Fe/H] $\lesssim -4.0$ dex the scatter of [Ca/Fe] increases (see, e.g., Francois et al. 2020). The (T, ρ) pairs in the opacity table match those of the atmosphere, avoiding interpolation. The tables include 100,000 frequency points, sampled logarithmically in wavelength between 900 and 100,000 Å, and were used in `Tlusty` for the calculation of the NLTE populations for Ca and Mg. Those populations were fed back to `Synspec` to produce detailed NLTE and LTE spectra to be compared with observations.[13]

[8] http://research.iac.es/proyecto/abundancias/horus/index.php
[9] Available from github.com/callendeprieto/chain.
[10] Based on data from the ESO Science Archive Facility. Program ID: 077.D-0035(A).
[11] Link to IAC cloud.
[12] Same link.
[13] The model atmospheres could have been computed by Tlusty as well, using an analogous full opacity table, but due to historical reasons (and for a comparison to previous studies), we have opted to stick with the ATLAS code.

Table 1
Stellar Parameters for the Synthetic Atmospheric Models Used in Our Comparison with Observations

Target	Instrument	$T_{\rm eff}$ (K)	$\log g$ (cm s^{-2})	[Fe/H] (dex)	[C/Fe] (dex)	[O/Fe] (dex)	$v_{\rm turb}$ (km s^{-1})	Parameters Source
G64-12	ISIS/HORuS	6390	4.4	−3.2	1.0	1.0	1.6	Aoki et al. (2006)
SDSS 134338	HORuS	5888	4.1	−3.3	1.0	1.0	1.5	Aguado et al. (2017)
HE 1327−2326	ISIS/UVES	6180	3.7	−5.6	4.0	3.0	1.7	Aoki et al. (2006)
HD 122563	UVES	4587	1.6	−2.6	1.0	1.0	1.0	Amarsi et al. (2016)

3.1. Model Atom

We adopted the model atom described in Osorio et al. (2019), with updates in the hydrogen interactions with Ca I and II presented by Belyaev et al. (2018). This update includes charge exchange between protons and calcium atoms and between H and singly ionized calcium.

The model atom has 66 levels for Ca I, 24 for Ca II, and the ground level of Ca III. These figures are different from those presented in Osorio et al. (2019) since, for this run, we merged all fine-structure components into single levels. This saves computing time without degrading accuracy.[14]

The radiative data used were the same as in Osorio et al. (2019). The transitions involving fine-structure components were merged accordingly (see Osorio et al. 2019, Section 2.1). This leads to 912 and 89 bound−bound transitions for Ca I and Ca II, respectively.

The electron collisional data are the same as in Osorio et al. (2019), i.e., Cox (2000), Bely & van Regemorter (1970), Vrinceanu (2005) for electron collisional ionization, while for electron collisional excitation we adopted Zatsarinny et al. (2019) and Seaton (1962) for Ca I and Meléndez et al. (2007) and Burgess et al. (1977) for Ca II.

In Osorio et al. (2019), hydrogen collisions were considered only for Ca I and neglected for Ca II. For Ca I + H, they used Barklem (2016, 2017) and Kaulakys (1986). In this work we also implemented charge exchange between Ca I and excited H($n = 2$), hydrogen collisional excitation of Ca II (for transitions involving levels up to $4f^2F^*$), and charge exchange with Ca II,

$$\text{Ca II} + \text{H} \Longleftrightarrow \text{Ca III} + \text{H}^-.$$

These new data come from Belyaev et al. (2018). The importance for this work of these new processes lies in the fact that we focus our study on Ca II features, and the new collisional data directly affect the statistical balance of the levels involved in these transitions.

We also studied Mg and Ca interspecies NLTE effects by simultaneously calculating NLTE populations of Mg and Ca (neutral and singly ionized), as in Osorio et al. (2020).

4. Results

For the three most metal-poor stars studied in this work, assuming LTE leads to overestimated calcium abundances. NLTE effects strengthen the Ca II lines, making their detection easier at lower calcium abundances. We also found negligible interspecies NLTE effects between calcium and magnesium. Only for the coolest model (SDSS 134338, $T_{\rm eff} = 5888$ K) are the populations of the highest levels of Ca II and the ground level of Ca III perturbed by a few percent owing to NLTE effects of Mg in the outermost atmospheric layers. Our observations do not include lines of Ca II involving those levels, but interspecies effects with other ions should be studied.

Using the HORuS observations of G64-12, we derived the calcium abundance in this star from three transitions: the Ca II H and K lines and Ca I λ4227 (see Table 2). The first thing to notice is the consistency between the Ca I and Ca II NLTE abundances. In the LTE case, the abundances from the Ca II resonance doublet are ≈0.1. dex greater than the values from the Ca I λ4227 transition.

We studied the effects of spectral resolution on the derived LTE abundances and NLTE abundance corrections for G64-12 and SDSS 134338. At the resolving power of HORuS ($R = 25{,}000$), the best-fitting NLTE profile for the Ca II K line reproduces more closely the observations than the LTE one. This is no longer the case at the lower resolution of the ISIS data, which are fit equally well in LTE and NLTE. The NLTE correction for this line doubles between HORuS and ISIS resolution: while the NLTE abundances derived from fitting the line profile are the same, the inferred LTE abundance increases between the HORuS and the ISIS best fittings. This is simply the result of lower resolution spreading the NLTE effects affecting the line core over a wider range of frequencies, enhancing the systematic error in the LTE-based abundance.

5. Formation Depth and Line Formation, the Case of HD 122563

We included HD 122563 in the analysis, the most metal-rich star in our sample, as illustrated in Table 1. We found that the core of Ca II H and K, Ca I λ4227, and the Ca II IR triplet lines form at layers beyond the limits of our model atmospheres ($log(\tau_{\rm ross}) = -6$), and special care must be taken for the derived abundances from these lines.

The core of the H and K and the λ4227 lines form at the top layers of our model atmospheres, but we expect those regions to be less realistic owing to NLTE effects on the structure of the atmospheres and temperature inversions that are not accounted for in standard models of late-type stellar atmospheres.

The dependency of the calculated line profile on the extension of the model atmosphere used in the calculation is most clear in the Ca I λ4227 line, shown in the middle panel of Figure 1. The core of this line is formed at $\log \tau_{\rm ross} \sim -6.0$ in LTE and at $\log \tau_{\rm ross} \sim -4.5$ in NLTE. The gf-value of this particular line comes from Hulpke et al. (1964) with an error of around 3% (0.013 dex for $\log gf$), which cannot explain the difference between the synthetic profile and observations.

NLTE corrections of strong lines computed by comparison of equivalent widths are sensitive to the extent of the stellar atmosphere because the core of the LTE profile of strong lines

[14] The calculations in Osorio et al. (2019) and other works showed that NLTE populations of fine-structure components of the same level share nearly identical departures from LTE and can be treated as a single level.

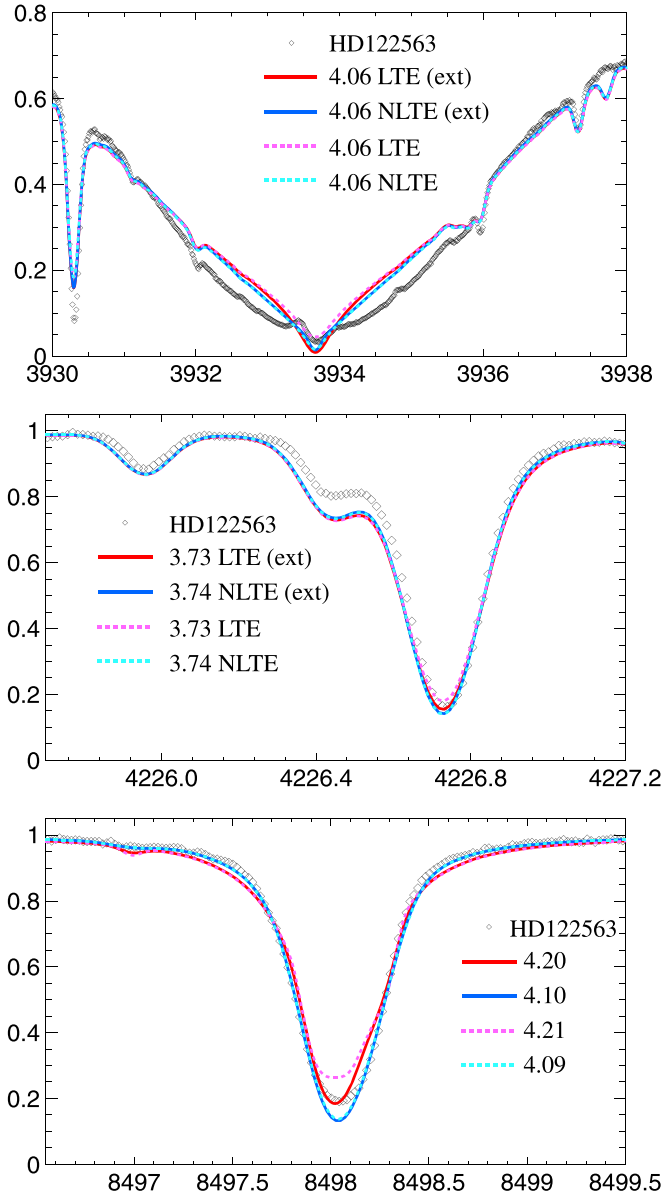

Figure 1. Comparison between UVES observations of HD 122563 and the best-fit LTE (red) and NLTE (blue) spectra for the Ca II K line (top), the Ca I λ4226 (middle), and the IR triplet member Ca II λ8498 line (bottom). Solid lines use an extended model atmosphere (min $\log \tau_{\rm ross} = -8.0$); light dashed lines go up to the standard depth (min $\log \tau_{\rm ross} = -5.0$).

gets deeper with more extended atmospheres, which does not happen with the NLTE profile.

It is known that the LTE approximation gradually loses validity with atmospheric height until it is no longer useful in the highest layers. Lines with weak wings and with cores that form at very high atmospheric layers (like the Ca I λ4227 line) should not be used for abundance determination because the region where the core forms is not modeled correctly owing to the extension of the model atmosphere and problems in the modeling of the highest layers of cool stellar atmospheres. These problems appear in both 1D and 3D atmospheric models.

6. Most Extreme Metal-poor Stars

For the other stars in this study, the cores of the Ca II H and K, the Ca I λ4227, and the Ca II IR triplet lines do not form at the highest layers, and therefore the differences between the LTE and NLTE line profiles cannot be attributed to the extent of the model atmospheres.

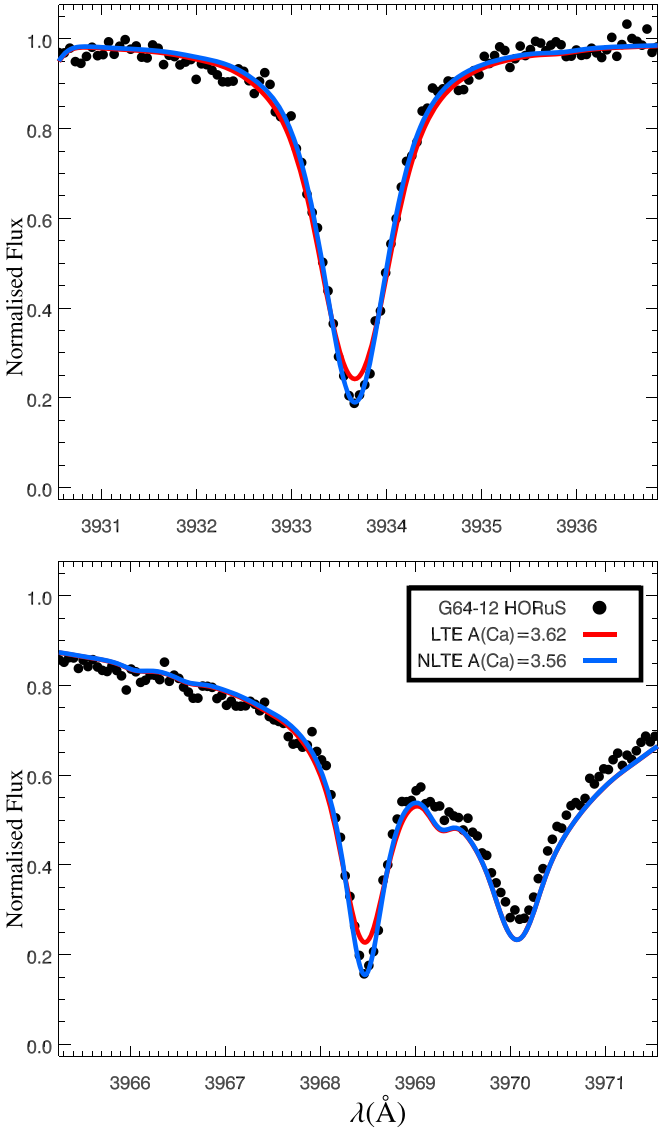

Figure 2. Comparison of the Ca II λ3934 and Ca II λ3969 (H and K) lines between HORuS observations of G64-12 (circles) and the best LTE (red) and NLTE (blue) fit. The Ca abundance used for each calculation is in the legend.

6.1. Ca II H and K Lines

The Ca II resonance lines are resolved in the HORuS observations of G64-12. The line profiles are nicely reproduced in NLTE, while in LTE the models miss absorption in the line cores, as illustrated in Figure 2.

The Ca I λ4266 line has been reported to give discrepant abundances compared to other Ca I lines when the line is strong (with an equivalent width $W_\lambda > 50$ mÅ; Mashonkina et al. 2007, 2017; Sitnova et al. 2019). This disagreement was reported in both LTE and NLTE analyses. We do not find this issue in our analysis of G64-12, where $W_\lambda \simeq 100$ mÅ. We derive an NLTE abundance correction of 0.1 dex, and our NLTE determination is consistent with the values from the other calcium lines, as can seen in Table 2. We believe that the reported discrepancy is related to the limited extension of the

Table 2
Calcium Abundances Inferred for Our Target Stars from the Individual Transitions

	Ca II λ3934		Ca II λ3968		Ca I λ4227		Ca II λ8497		Ca II 8542		Ca II 8662	
Star	LTE	NLTE	LTE	NLTE	LTE	NLTE	LTE	NLTE	LTE	NLTE	LTE	NLTE
HD 122563	4.06(05)	4.06(04)			3.73(05)	3.74(05)	4.20(05)	4.10(04)				
G64-12	3.64(06)	3.60(04)	3.66(09)	3.57(06)	3.53(12)	3.63(09)	4.08(12)	3.63(09)	4.04(10)	3.61(11)	4.11(10)	3.64(12)
SDSS 134338	3.42(04)	3.41(03)			3.35(07)	3.40(07)	3.82(08)	3.38(06)	3.80(06)	3.41(06)	3.85(11)	3.42(11)
HE 1327−2326	1.31(11)	1.15(09)	1.32(30)	1.11(21)					1.22(24)	1.16(19)		

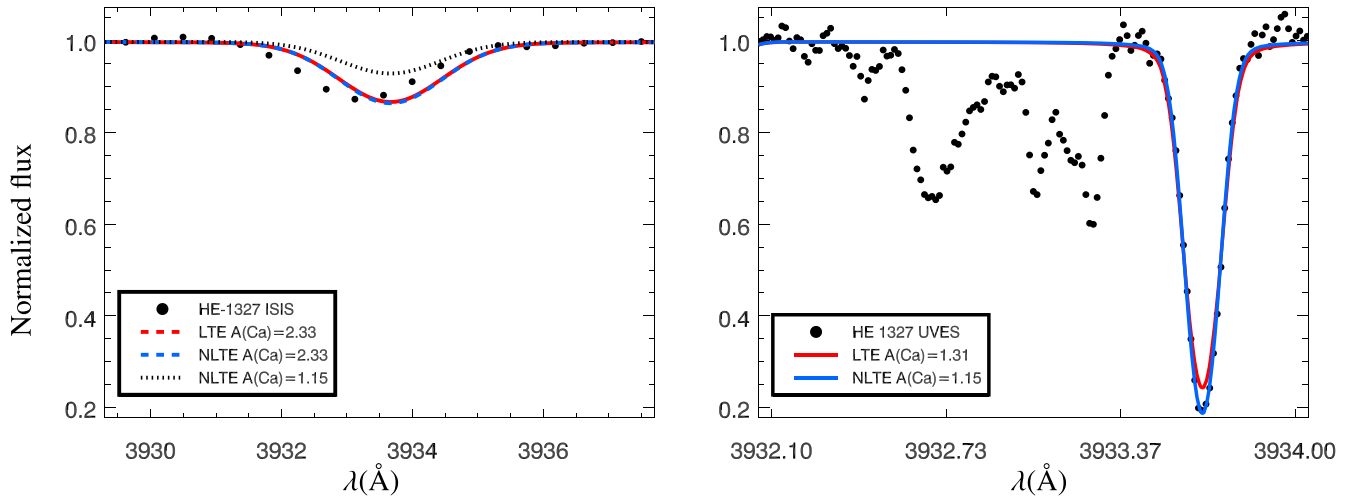

Figure 3. Ca LTE and NLTE synthetic profile vs. observations with ISIS ($R = 2000$; left) and UVES ($R = 40{,}000$; right) of the Ca II K line in HE 1327−2326. The inner plot in the left panel is a zoom-in on the Ca II λ3930 line and the ISIS observations. The Ca abundances used in the synthetic spectra calculations are written in the legends.

atmospheric models used by Mashonkina et al. (2007, 2017) and Sitnova et al. (2019). The core of the resonance lines forms in very high layers of the photosphere, and the Kurucz model atmospheres we adopt typically reach optical depths two orders of magnitude smaller than the MARCS model atmospheres used in those previous studies, as discussed by Osorio et al. (2019).

At the resolving power of HORuS, we cannot find signs of contamination from the ISM in the spectra of G64-12. For this star the Ca II resonance lines and the IR triplet treated in NLTE lead to consistent calcium abundances, while an LTE analysis of the triplet results in a discrepancy of 0.4 dex.

The UVES observations of HE 1327 show at least three lines blueshifted from the stellar Ca II H and K lines, as illustrated for the K line in the right panel of Figure 3. The LTE and NLTE best fittings for these lines give an NLTE abundance correction[15] of −0.15 dex for this star. At the lower resolution of the ISIS data, the interstellar components are blended with the stellar K line (left panel). Ignoring the ISM contribution would lead to a higher calcium abundance by more than 1.0 dex.

The dotted line in the left panel of Figure 3 shows the NLTE line profile of the K line using the NLTE abundance derived from the UVES observations (right panel) at the resolution of ISIS. By looking at the UVES observations, one would expect the W_λ of the resulting blend at ISIS resolution to have around twice the value of the stellar component alone. If the K line were in the linear region of the curve of growth in this star, we would expect an increase in abundance of ∼0.5 dex. The strength of the line at the resolution of UVES shows that this line is saturated.

6.2. Ca II IR Triplet

The IR triplet lines do not suffer from ISM contamination, but the levels involved in the IR triplet transitions ($3d\,^2D$–$4p\,^2P^o$), the first two excited levels of Ca II, are more suitable to exhibit populations that differ from LTE predictions. There are ISIS observations of these lines for all three stars studied in this work. The LTE and NLTE values are significantly different, and in all cases our derived NLTE abundances exhibit less dispersion than the LTE ones.

The NLTE corrections for the IR triplet in G64-12 and SDSS 134338 are ∼−0.4 dex. The NLTE abundances are consistent with those from other calcium lines. In contrast, the derived LTE abundances for these lines are higher.

There are multiple factors that complicate the abundance determination from the Ca II IR triplet lines. Two of those lines (λλ8497, 8662) are on the blue wings of hydrogen lines that are stronger than the calcium lines. The limited S/N of the ISIS data makes the same two lines lie within the noise level. Thus, for HE 1327, we derived the calcium abundance only from the λ8542 line. The NLTE abundance correction in this case is small, about 0.05 dex.

We performed NLTE calculations on a small grid (4500 K $\leqslant T_{\rm eff} \leqslant$ 6000 K, $\Delta = 500$ K; $1.0 \leqslant \log g \leqslant 4.0$, $\Delta = 1.0$ dex; −6.0 dex < [Fe/H] < −2.5 dex, $\Delta = 0.5$ dex) and present together with this work abundance corrections ΔA(Ca) for the triplet IR lines (see Table 3).

[15] Defined here as $\Delta A(\mathrm{Ca}) = A(\mathrm{Ca})_{\rm NLTE} - A(\mathrm{Ca})_{\rm LTE}$.

Table 3
NLTE Abundance Corrections of Ca Derived from the Three Lines of the Ca II IR Triplet for a Small Grid

$T_{\rm eff}$	log g	Fe/H	8498 Å	8542 Å	8662 Å
4500	1.0	−2.5	−0.171	−0.224	−0.175
4500	1.0	−3.0	−0.158	−0.122	−0.135
4500	1.0	−3.5	−0.152	−0.114	−0.140
4500	1.0	−4.0	−0.222	−0.191	−0.213
4500	1.0	−4.5	−0.276	−0.298	−0.311
4500	1.0	−5.0	−0.349	−0.430	−0.424
4500	1.0	−5.5	−0.412	−0.554	−0.526
4500	1.0	−6.0	−0.383	−0.609	−0.575
4500	2.0	−2.5	−0.195	−0.290	−0.222
4500	2.0	−3.0	−0.155	−0.143	−0.146
4500	2.0	−3.5	−0.112	−0.083	−0.100
4500	2.0	−4.0	−0.202	−0.159	−0.183
4500	2.0	−4.5	−0.246	−0.247	−0.262
4500	2.0	−5.0	−0.291	−0.353	−0.349
4500	2.0	−5.5	−0.295	−0.454	−0.436
4500	2.0	−6.0	−0.283	−0.499	−0.454
4500	3.0	−2.5	−0.208	−0.423	−0.293
4500	3.0	−3.0	−0.161	−0.201	−0.180
4500	3.0	−3.5	−0.160	−0.148	−0.157
4500	3.0	−4.0	−0.188	−0.168	−0.180
4500	3.0	−4.5	−0.218	−0.226	−0.233
4500	3.0	−5.0	−0.223	−0.297	−0.293
4500	3.0	−5.5	−0.220	−0.354	−0.327
4500	3.0	−6.0	−0.222	−0.323	−0.278
4500	4.0	−2.5	−0.232	−0.546	−0.371
4500	4.0	−3.0	−0.178	−0.281	−0.234
5000	1.0	−2.5	−0.272	−0.248	−0.244
5000	1.0	−3.0	−0.280	−0.214	−0.253
5000	1.0	−3.5	−0.283	−0.255	−0.292
5000	1.0	−4.0	−0.293	−0.337	−0.351
5000	1.0	−4.5	−0.287	−0.427	−0.418
5000	1.0	−5.0	−0.348	−0.560	−0.522
5000	1.0	−5.5	−0.336	−0.624	−0.571
5000	1.0	−6.0	−0.276	−0.610	−0.537
5000	2.0	−2.5	−0.310	−0.294	−0.294
5000	2.0	−3.0	−0.318	−0.261	−0.303
5000	2.0	−3.5	−0.329	−0.296	−0.331
5000	2.0	−4.0	−0.317	−0.364	−0.382
5000	2.0	−4.5	−0.302	−0.458	−0.444
5000	2.0	−5.0	−0.271	−0.523	−0.479
5000	2.0	−5.5	−0.220	−0.544	−0.481
5000	2.0	−6.0	−0.194	−0.456	−0.352
5000	3.0	−2.5	−0.283	−0.344	−0.304
5000	3.0	−3.0	−0.288	−0.259	−0.279
5000	3.0	−3.5	−0.297	−0.260	−0.287
5000	3.0	−4.0	−0.280	−0.303	−0.318
5000	3.0	−4.5	−0.227	−0.361	−0.349
5000	3.0	−5.0	−0.154	−0.395	−0.357
5000	3.0	−5.5	−0.136	−0.366	−0.285
5000	3.0	−6.0	−0.131	−0.233	−0.179
5000	4.0	−2.5	−0.240	−0.422	−0.314
5000	4.0	−3.0	−0.228	−0.252	−0.243
5000	4.0	−3.5	−0.223	−0.220	−0.228
5000	4.0	−4.0	−0.047	−0.080	−0.070
5000	4.0	−4.5	−0.127	−0.254	−0.239
5000	4.0	−5.0	−0.096	−0.242	−0.196
5000	4.0	−5.5	−0.089	−0.157	−0.121
5000	4.0	−6.0	−0.083	−0.106	−0.091
5500	1.0	−2.5	−0.302	−0.244	−0.268
5500	1.0	−3.0	−0.310	−0.263	−0.305
5500	1.0	−3.5	−0.312	−0.332	−0.360
5500	1.0	−4.0	−0.295	−0.413	−0.418
5500	1.0	−4.5	−0.294	−0.515	−0.490
5500	1.0	−5.0	−0.301	−0.600	−0.544

Table 3
(Continued)

$T_{\rm eff}$	log g	Fe/H	8498 Å	8542 Å	8662 Å
5500	1.0	−5.5	−0.255	−0.628	−0.557
5500	1.0	−6.0	−0.196	−0.516	−0.407
5500	2.0	−2.5	−0.363	−0.302	−0.341
5500	2.0	−3.0	−0.377	−0.342	−0.390
5500	2.0	−3.5	−0.375	−0.414	−0.440
5500	2.0	−4.0	−0.333	−0.491	−0.492
5500	2.0	−4.5	−0.292	−0.565	−0.521
5500	2.0	−5.0	−0.230	−0.587	−0.521
5500	2.0	−5.5	−0.179	−0.536	−0.438
5500	2.0	−6.0	−0.140	−0.317	−0.231
5500	3.0	−2.5	−0.350	−0.318	−0.345
5500	3.0	−3.0	−0.383	−0.345	−0.383
5500	3.0	−3.5	−0.380	−0.404	−0.430
5500	3.0	−4.0	−0.329	−0.473	−0.471
5500	3.0	−4.5	−0.222	−0.505	−0.463
5500	3.0	−5.0	−0.143	−0.481	−0.407
5500	3.0	−5.5	−0.118	−0.337	−0.236
5500	3.0	−6.0	−0.093	−0.157	−0.123
5500	4.0	−2.5	−0.279	−0.306	−0.296
5500	4.0	−3.0	−0.301	−0.287	−0.303
5500	4.0	−3.5	−0.294	−0.311	−0.326
5500	4.0	−4.0	−0.226	−0.346	−0.340
5500	4.0	−4.5	−0.113	−0.346	−0.305
5500	4.0	−5.0	−0.075	−0.266	−0.189
5500	4.0	−5.5	−0.056	−0.119	−0.085
5500	4.0	−6.0	−0.034	−0.055	−0.041
6000	2.0	−2.5	−0.386	−0.340	−0.395
6000	2.0	−3.0	−0.397	−0.419	−0.466
6000	2.0	−3.5	−0.370	−0.502	−0.523
6000	2.0	−4.0	−0.320	−0.577	−0.561
6000	2.0	−4.5	−0.265	−0.627	−0.568
6000	2.0	−5.0	−0.201	−0.624	−0.548
6000	2.0	−5.5	−0.142	−0.455	−0.342
6000	2.0	−6.0	−0.098	−0.200	−0.154
6000	3.0	−2.5	−0.398	−0.364	−0.417
6000	3.0	−3.0	−0.419	−0.442	−0.481
6000	3.0	−3.5	−0.383	−0.525	−0.544
6000	3.0	−4.0	−0.312	−0.592	−0.561
6000	3.0	−4.5	−0.199	−0.589	−0.521
6000	3.0	−5.0	−0.143	−0.514	−0.407
6000	3.0	−5.5	−0.100	−0.253	−0.179
6000	3.0	−6.0	−0.061	−0.101	−0.083
6000	4.0	−2.5	−0.321	−0.312	−0.335
6000	4.0	−3.0	−0.342	−0.362	−0.385
6000	4.0	−3.5	−0.316	−0.429	−0.435
6000	4.0	−4.0	−0.216	−0.470	−0.438
6000	4.0	−4.5	−0.117	−0.432	−0.354
6000	4.0	−5.0	−0.088	−0.283	−0.192
6000	4.0	−5.5	−0.056	−0.107	−0.080
6000	4.0	−6.0	−0.016	−0.033	−0.022
6500	3.0	−2.5	−0.407	−0.430	−0.494
6500	3.0	−3.0	−0.395	−0.524	−0.570
6500	3.0	−3.5	−0.345	−0.609	−0.618
6500	3.0	−4.0	−0.271	−0.658	−0.612
6500	3.0	−4.5	−0.178	−0.630	−0.554
6500	3.0	−5.0	−0.126	−0.464	−0.346
6500	3.0	−5.5	−0.075	−0.170	−0.134
6500	3.0	−6.0	−0.022	−0.049	−0.041
6500	4.0	−2.5	−0.333	−0.362	−0.394
6500	4.0	−3.0	−0.327	−0.442	−0.464
6500	4.0	−3.5	−0.279	−0.520	−0.504
6500	4.0	−4.0	−0.178	−0.539	−0.479
6500	4.0	−4.5	−0.062	−0.263	−0.190
6500	4.0	−5.0	−0.089	−0.243	−0.169

Table 3
(Continued)

$T_{\rm eff}$	log g	Fe/H	8498 Å	8542 Å	8662 Å
6500	4.0	−5.5	−0.042	−0.071	−0.058
6500	4.0	−6.0	0.010	−0.004	0.005
7000	4.0	−2.5	−0.312	−0.424	−0.465
7000	4.0	−3.0	−0.282	−0.509	−0.523
7000	4.0	−3.5	−0.218	−0.565	−0.527
7000	4.0	−4.0	−0.112	−0.462	−0.396
7000	4.0	−4.5	−0.100	−0.398	−0.288
7000	4.0	−5.0	−0.073	−0.176	−0.136
7000	4.0	−5.5	−0.028	−0.057	−0.050
7000	4.0	−6.0	0.065	0.053	0.062

Note. The first three columns are $T_{\rm eff}$, log g, and [Fe/H], respectively; the last three columns are the abundance corrections ΔA(Ca) for each of the IR Ca II triplet lines.

7. Conclusions

Absorption produced in the ISM can lead to systematic errors in the determination of stellar abundances of calcium from the Ca II resonance lines. The Ca II IR triplet offers an alternative way of measuring the metallicity of these stars, free from ISM absorption, but afflicted by significant departures from LTE. Earlier analysis reported inconsistencies between the abundances derived from these transitions, as well as those from neutral calcium lines, and we consider whether recent updates in the data available for the relevant physical processes have improved the situation.

We perform Mg+Ca multispecies NLTE (NLTE-m) calculations, including the most relevant collisional processes. The new H+Ca^+ collisional data from Belyaev et al. (2018) do have significant effects on our NLTE calculations. NLTE effects strengthen the core of the Ca II infrared triplet lines, reducing the inferred abundance, and getting it into agreement with the values from the resonance lines, mostly free from NLTE effects, whenever the latter can be isolated from ISM contributions.

We conclude that our state-of-the-art NLTE calculations, similarly to those recently published by Sitnova et al. (2019), are mature enough to standardize the use of the Ca II IR triplet to infer reliably the calcium abundance in very metal-poor stars from medium-resolution observations. Furthermore, we make public all the necessary data and tools for anyone to repeat and extend our calculations to any other star.

Together with this paper, we release scripts, line lists, model atoms, and the versions of `Tlusty/Synspec` deployed for this work (Hubeny et al. 2021). Additional calculations are possible by running these scripts.

This paper is focused on NLTE; however, it is well known that 3D effects can be important for the accurate inference of atmospheric parameters and the abundances of some species at low metallicity (Asplund 2005; Ruchti et al. 2013; Amarsi et al. 2016; Nordlander et al. 2019). G64-12 in particular was analyzed by Bergemann et al. (2012) in NLTE using MARCS and *horizontally averaged* 3D atmospheres, and this star and HD 122563 were studied by Amarsi et al. (2016) using full 3D NLTE. Serenelli et al. (2013) include a useful discussion of the influence of LTE and NLTE model atmospheres in the Ca near-IR triplet lines at low metallicity.

Our conclusions, together with the actual data and tools to extend our calculations to other stars, have important implications for the discovery of extremely metal-poor stars in the new future. As demonstrated in this paper, the triplet can be reliably used to infer stellar metallicities in these stars when departures from LTE are accounted for. In addition, Nordlander et al. (2017) have shown that 3D effects are not likely to change the calcium abundances derived in 1D from Ca II lines in extremely metal-poor stars by more than 0.1 dex.

Several massive spectroscopic surveys of the Milky Way covering the Ca II infrared lines are underway or close to starting (SDSS, LAMOST, DESI, WEAVE, PFS, etc.). Next year the 3rd Gaia Data Release will make public millions of $R \simeq 11{,}500$ spectra covering the Ca II IR triplet. The tools presented in this paper can be used to mine with confidence these data for identifying new extremely metal-poor stars.

We thank the referee for his/her valuables remarks and suggestions during the referring process. Y.O., C.A.P., and J.I. G.H. acknowledge financial support from the Spanish Ministry of Science and Innovation (MICINN) under the FEDER Agreement INSIDE-OOCC (ICTS-2019-03-IAC-12) and from the Spanish MICINN project AYA2017-86389-P. D.A. thanks the Leverhulme Trust for financial support. D.A. acknowledges support from ERC Starting Grant NEFERTITI H2020/808240. Based on observations made with the William Herschel Telescope (WHT) and the Gran Telescopio Canarias (GTC), installed in the Spanish Observatorio del Roque de los Muchachos of the Instituto de Astrofísica de Canarias, on the island of La Palma.

ORCID iDs

Yeisson Osorio https://orcid.org/0000-0001-5832-6933
David S. Aguado https://orcid.org/0000-0001-5200-3973
Carlos Allende Prieto https://orcid.org/0000-0002-0084-572X
Ivan Hubeny https://orcid.org/0000-0001-8816-236X
Jonay I. González Hernández https://orcid.org/0000-0002-0264-7356

References

Aguado, D. S., Allende Prieto, C., González Hernández, J. I., et al. 2016, A&A, 593, A10
Aguado, D. S., Allende Prieto, C., González Hernández, J. I., & Rebolo, R. 2018a, ApJL, 854, L34
Aguado, D. S., González Hernández, J. I., Allende Prieto, C., & Rebolo, R. 2017, A&A, 605, A40
Aguado, D. S., González Hernández, J. I., Allende Prieto, C., & Rebolo, R. 2018b, ApJL, 852, L20
Allende Prieto, C. 2021, NatAs, 5, 105
Amarsi, A. M., Lind, K., Asplund, M., Barklem, P. S., & Collet, R. 2016, MNRAS, 463, 1518
Aoki, W., Frebel, A., Christlieb, N., et al. 2006, ApJ, 639, 897
Asplund, M. 2005, ARA&A, 43, 481
Barklem, P. S. 2016, PhRvA, 93, 042705
Barklem, P. S. 2017, PhRvA, 95, 069906
Beers, T. C., Preston, G. W., & Shectman, S. A. 1985, AJ, 90, 2089
Bely, O., & van Regemorter, H. 1970, ARA&A, 8, 329
Belyaev, A. K., Voronov, Y. V., & Gadéa, F. X. 2018, ApJ, 867, 87
Belyaev, A. K., Voronov, Y. V., Yakovleva, S. A., et al. 2017, ApJ, 851, 59
Bergemann, M., Lind, K., Collet, R., Magic, Z., & Asplund, M. 2012, MNRAS, 427, 27
Bonifacio, P., Caffau, E., Spite, M., et al. 2015, A&A, 579, A28
Bromm, V., & Loeb, A. 2003, Natur, 425, 812
Burgess, A., Summers, H. P., McWhirter, R. W. P., & Cochrane, D. M. 1977, MNRAS, 179, 275
Caffau, E., Bonifacio, P., Sbordone, L., et al. 2013, A&A, 560, A71
Chiaki, G., Tominaga, N., & Nozawa, T. 2017, MNRAS, 472, L115

Christlieb, N., Gustafsson, B., Korn, A. J., et al. 2004, ApJ, 603, 708
Cox, A. N. 2000, Allen's Astrophysical Quantities (Berlin: Springer)
Cropper, M., Katz, D., Sartoretti, P., et al. 2018, A&A, 616, A5
Dekker, H., D'Odorico, S., Kaufer, A., Delabre, B., & Kotzlowski, H. 2000, Proc. SPIE, 4008, 534
François, P., Wanajo, S., Caffau, E., et al. 2020, A&A, 642, A25
Frebel, A., Aoki, W., Christlieb, N., et al. 2005, Natur, 434, 871
García Pérez, A. E., Asplund, M., Primas, F., Nissen, P. E., & Gustafsson, B. 2006, A&A, 451, 621
Hartwig, T., Yoshida, N., Magg, M., et al. 2018, MNRAS, 478, 1795
Heiter, U., Jofré, P., Gustafsson, B., et al. 2015, A&A, 582, A49
Hubeny, I., Allende-Prieto, C., Osorio, Y., & Lanz, T. 2021, arXiv:2102.01937
Hubeny, I., & Lanz, T. 2017a, arXiv:1706.01859
Hubeny, I., & Lanz, T. 2017b, arXiv:1706.01935
Hubeny, I., & Lanz, T. 2017c, arXiv:1706.01937
Hulpke, E., Paul, E., & Paul, W. 1964, Zeitschrift für Physik, 177, 257
Ishigaki, M. N., Tominaga, N., Kobayashi, C., & Nomoto, K. 2014, ApJL, 792, L32
Jorden, P. R. 1990, Proc. SPIE, 1235, 790
Kaulakys, B. P. 1986, JETP, 91, 391
Keller, S. C., Bessell, M. S., Frebel, A., et al. 2014, Natur, 506, 463
Komiya, Y., Suda, T., & Fujimoto, M. Y. 2016, ApJ, 820, 59
Kurucz, R. L. 2005, MSAIS, 8, 14
Magg, M., Hartwig, T., Agarwal, B., et al. 2018, MNRAS, 473, 5308
Mashonkina, L., Korn, A. J., & Przybilla, N. 2007, A&A, 461, 261
Mashonkina, L., Sitnova, T., & Belyaev, A. K. 2017, A&A, 605, A53
Meléndez, M., Bautista, M. A., & Badnell, N. R. 2007, A&A, 469, 1203
Nordlander, T., Amarsi, A. M., Lind, K., et al. 2017, A&A, 597, A6
Nordlander, T., Bessell, M. S., Da Costa, G. S., et al. 2019, MNRAS, 488, L109
Osorio, Y., Allende Prieto, C., Hubeny, I., Mészáros, S., & Shetrone, M. 2020, A&A, 637, A80
Osorio, Y., Lind, K., Barklem, P., Allende-Prieto, C., & Zatsarinny, O. 2019, A&A, 623, 17
Ruchti, G. R., Bergemann, M., Serenelli, A., Casagrande, L., & Lind, K. 2013, MNRAS, 429, 126
Sbordone, L., Bonifacio, P., & Castelli, F. 2007, in Convection in Astrophysics, Proc. of IAU Symp. 239, ed. F. Kupka, I. Roxburgh, & K. L. Chan (Cambridge: Cambridge Univ. Press), 71
Seaton, M. J. 1962, in Atomic and Molecular Processes, ed. D. R. Bates (Cambridge, MA: Academic Press), 375
Serenelli, A. M., Bergemann, M., Ruchti, G., & Casagrande, L. 2013, MNRAS, 429, 3645
Sitnova, T. M., Mashonkina, L. I., Ezzeddine, R., & Frebel, A. 2019, MNRAS, 485, 3527
Stacy, A., Bromm, V., & Lee, A. T. 2016, MNRAS, 462, 1307
Tabernero, H. M., Allende Prieto, C., Zapatero Osorio, M. R., et al. 2020, MNRAS, 498, 4222
Umeda, H., & Nomoto, K. 2005, ApJ, 619, 427
Vrinceanu, D. 2005, PhRvA, 72, 022722
Zatsarinny, O., Parker, H., & Bartschat, K. 2019, PhRvA, 99, 012706